Published in final edited form as:

Nature. 2017 July 06; 547(7661): 68–73. doi:10.1038/nature22354.

Single-molecule analysis of ligand efficacy in β_2AR-G protein activation

G. Glenn Gregorio[1,*], **Matthieu Masureel**[2,*], **Daniel Hilger**[2,*], **Daniel S. Terry**[1], **Manuel Juette**[1], **Hong Zhao**[1], **Zhou Zhou**[1], **Jose Manuel Perez-Aguilar**[1,9], **Maria Hauge**[3,5,7,8], **Signe Mathiasen**[3,5], **Jonathan A. Javitch**[3,4,5], **Harel Weinstein**[1,6], **Brian K. Kobilka**[2,‡], and **Scott C. Blanchard**[1,‡]

[1]Department of Physiology and Biophysics, Weill Cornell Medicine, New York, New York, USA

[2]Department of Molecular and Cellular Physiology, Stanford University School of Medicine, Stanford, California, USA

[3]Department of Psychiatry, Columbia University College of Physicians and Surgeons, New York, New York, USA

[4]Department of Pharmacology, Columbia University College of Physicians and Surgeons, New York, New York, USA

[5]Division of Molecular Therapeutics, New York State Psychiatric Institute, New York, New York, USA

[6]The HRH Prince Alwaleed Bin Talal Bin Abdulaziz Alsaud Institute for Computational Biomedicine, Weill Cornell Medical College of Cornell University, New York, New York, USA

[7]Laboratory for Molecular Pharmacology, Department of Neuroscience and Pharmacology, University of Copenhagen, Blegdamsvej 3, Copenhagen 2200, Denmark

[8]NNF Center for Basic Metabolic Research, University of Copenhagen, Blegdamsvej 3, Copenhagen 2200, Denmark

SUMMARY

‡Correspondence should be addressed to B.K.K. (kobilka@stanford.edu) and S.C.B. (scb2005@med.cornell.edu).
[9]Present address: IBM Thomas J. Watson Research Center, Yorktown Heights, New York 10598, USA
*These authors contributed equally to this work.
Correspondence and requests for materials should be addressed to B.K.K. (kobilka@stanford.edu) and S.C.B. (scb2005@med.cornell.edu).

Data availability. The data that support the findings of this study are available from the corresponding author upon reasonable request.

Author Contributions. G.G.G., M.M., D.H., B.K.K. and S.C.B. designed single-molecule experiments. G.G.G. labeled receptor and performed all single-molecule experiments. G.G.G. analyzed single-molecule data, with support from D.S.T. M.J. and D.S.T. developed the imaging and analysis platform. M.M. expressed, purified and characterized receptor constructs. D.H. expressed, purified and biotinylated G_S, and performed GTP turnover assays. H.Z. and Z.Z. synthesized the fluorophores. J.M.P-A. performed MD simulations under supervision of H.W. M.H. and S.M. performed cell-based G protein-coupling assays under supervision of J.A.J.. G.G.G., M.M., D.H., J.A.J., H.W., B.K.K., and S.C.B. interpreted all the data and wrote the manuscript. B.K.K. and S.C.B. provided overall project supervision.

The authors declare competing financial interest: details accompany the full-text HTML version of the paper (nature.com).

G protein-coupled receptor (GPCR)-mediated signal transduction is central to human physiology and disease intervention, yet the molecular mechanisms responsible for ligand-dependent signaling responses remain poorly understood. In Class A GPCRs, receptor activation and G protein coupling entail outward movements of transmembrane segment 6 (TM6). Using single-molecule Fluorescence Resonance Energy Transfer (smFRET) imaging, we examine TM6 motions in the β_2 adrenergic receptor (β_2AR) upon exposure to orthosteric ligands with different efficacies, in the absence and presence of the G_s heterotrimer. We show that partial and full agonists affect TM6 motions in a manner that differentially regulates the rate at which GDP-bound β_2AR-G_s complexes are formed and the efficiency of nucleotide exchange leading to G_s activation. These data also reveal transient nucleotide-bound β_2AR-G_s species distinct from known structures and single-molecule perspectives on the allosteric link between ligand and nucleotide binding pockets that shed new light on the G protein activation mechanism.

GPCRs regulate cellular responses to neurotransmitters and hormones and act as ligand-regulated guanosine nucleotide exchange factors (GEFs) for heterotrimeric G proteins[1]. Ligand efficacy has historically referred to a molecule's capacity to elicit a specific physiological response downstream of receptor activation[2,3]. Although an important parameter in drug development, the molecular basis of efficacy with respect to a ligand's impact on GPCR structure, dynamics and G protein coupling remains poorly understood.

The β_2 adrenergic receptor (β_2AR), a paradigmatic, Class A GPCR couples preferentially to the heterotrimeric G_s protein, comprised of $G\alpha_s$, $G\beta$ and $G\gamma$ (Fig. 1a)[4]. Investigations of the β_2AR activation mechanism have been enabled by synthetic ligands with efficacy profiles ranging from inverse agonists that suppress basal activity, and neutral antagonists that prevent agonist-induced activation, to partial and full agonists that differentially promote receptor-mediated G_s activation[5]. Recent crystallographic structures of distinct Class A GPCRs in both inactive and active states[6–9] revealed that the largest conformational change associated with their activation is an outward movement of the cytoplasmic end of transmembrane helix 6 (TM6)[6]. In the nucleotide-free β_2AR-G_s complex, TM6 is stabilized in an outward configuration by insertion of the C-terminal α5 helix of $G\alpha_s$ into a pocket formed by the cytoplasmic ends of TM3, TM5 and TM6 and intracellular loop 2 (ICL2).

Ensemble techniques, including fluorescence[10], electron paramagnetic resonance (EPR)[11] and nuclear magnetic resonance (NMR) spectroscopy[11,12] reveal that even the most potent agonists fail to fully stabilize β_2AR in its activated conformation in the absence of G protein or stabilizing nanobodies. The molecular basis of ligand efficacy may therefore be defined by changes in receptor dynamics and conformation that impact the probability of G-protein coupling, productive nucleotide exchange and subsequent dissociation. Hence, we used total internal reflection fluorescence (TIRF) smFRET imaging to track TM6 movements in β_2AR bound to ligands with distinct efficacy profiles to determine the impacts on receptor structure, dynamics, and G protein coupling.

Site-specific labeling of β_2AR

We site-specifically attached donor and acceptor fluorescent probes at the cytoplasmic ends of TM6 (L266C$^{6.28}$) and TM4 (N148C$^{4.40}$), respectively, within a full-length, minimal

cysteine β_2AR mutant (Fig. 1a; **Methods**). This construct ($\beta_2\Delta$6-148C/266C) exhibits wild-type ligand binding and G_s coupling (Extended Data Fig. 1a–c).

Given β_2AR's relatively small size (~34Å lateral dimension) and TM6's anticipated displacement (~14Å) upon activation (Fig. 1a)[6], $\beta_2\Delta$6-148C/266C was labeled with an optimized Cy3B and Cy7 fluorophore pair (Cy3B* and Cy7*, Extended Data Figs. 2a,b and 3a,b; **Methods**), which exhibit high quantum yields and a small R_0 (~50.7Å) (Extended Data Fig. 2a–e) and should be relatively insensitive to chemical environment[13]. Labeled receptors showed wild-type activities with respect to both antagonist and agonist binding (Extended Data Fig. 1a,b).

Ligand-induced TM6 displacement

The impacts of saturating concentrations of nine ligands with distinct efficacies (Fig. 1b, Extended Data Fig. 1d,e) were examined by imaging Cy3B*/Cy7*-labeled $\beta_2\Delta$6-148C/266C immobilized with an M1 Fab fragment (Fig. 2a,b; Extended Data Figs. 3c and 4a,b). In the presence of the neutral antagonist alprenolol (alp), the inverse agonists carazolol (cz), and ICI-118,151 (ICI), β_2AR exhibited indistinguishable population FRET efficiencies (FRET) centered at 0.74±0.01 (~0.74) and full-widths at half maximum height (FWHM) of 0.1±0.01 (~0.1; mean of biological replicates ±s.d.) (Fig. 2b). Inspection of individual trajectories from alp-, cz- and ICI-bound receptors revealed relatively stable fluorescence and FRET (Extended Data Fig. 4a). Similar results were obtained when β_2AR was immobilized *via* biotinylated alp (Extended Data Fig. 3d,e). These data predict an average inter-dye distance of approximately 42Å (Extended Data Fig. 2d–f), in good agreement with molecular dynamics (MD) simulations (Extended Data Fig. 5a,b).

The unliganded (apo) β_2AR exhibited a mean FRET value and FWHM similar to that of alp, cz, and ICI (Fig. 2b). In the presence of the partial agonists clenbuterol (clen), salmeterol (salm) or salbutamol (salb), β_2AR exhibited modestly lower, and more broadly distributed FRET values (~0.70–0.72; FWHM:~0.15) (Fig. 2b). Reductions in FRET were more pronounced in the presence of the full agonists epinephrine (epi), isoproterenol (iso) and BI-167107 (BI), where the mean FRET value shifted to ~0.64 (FWHM:~0.15) (Fig. 2b). In agreement with radioligand binding studies (Extended Data Fig. 1e), smFRET experiments showed that epi exhibited a half-maximum effective concentration (EC_{50}) of 0.48±0.09 μM (mean of biological replicates ±s.e.m.) (Fig. 2c; Extended Data Fig. 3f). Hence, we infer that these epi-induced FRET changes ($\Delta FRET_{apo/epi}$:~0.1), corresponding to an increase in average interdye distance of ~4Å (Extended Data Fig. 2e), reflect those of a fully functional receptor.

While the ~14Å outward TM6 movement observed in fully activated β_2AR (Fig. 1a; Extended Data Fig. 5) is anticipated to yield a FRET change of ~0.3 (Extended Data Fig. 2e), inspection of individual FRET trajectories revealed only rare fluctuations (ca. 1 min^{-1}) of this amplitude (Extended Data Fig. 4a). However, correlation analyses[14,15] revealed clear signatures of anticorrelated fluorescence within the ensemble of individual molecules (Fig. 2d–f; Extended Data Fig. 4c–e; **Methods**), indicating fast (>10 s^{-1}), reversible TM6 movements. By this measure, more rapid TM6 dynamics (more negative mean correlation)

were observed in agonist-bound samples than antagonist-bound samples (Fig 2e,f). Simulations revealed that the observed fluorescence correlation and FRET distributions could be recapitulated by TM6 deflections to lower FRET states at rates of 100–500 s^{-1} (Extended Data Fig. 4d,e). Previous reports of slower TM6 movements (ca.~0.5–5 s^{-1})[11,16] may reflect differences in experimental conditions or the nature of their probes, which detect changes in environment, not distance. Hence, we conclude that the distinct FRET values observed for each agonist reflect differences in the underlying rates and/or amplitudes of TM6 motions into, and out of, active-like conformations, which are time averaged at the present imaging resolution.

The rate of β_2AR-G_s complex formation

To ascertain directly the extent to which the ligand-induced changes observed in smFRET correlate with the coupling efficiency of β_2AR to G protein, labeled β_2AR (1 nM) was incubated with G_s (8 μM) and apyrase (0.2 nM). Individual β_2AR molecules were subsequently imaged *via* M1 immobilization to determine the extent of β_2AR-G_s complex formation (Fig. 3a).

In the presence of cz and ICI, β_2AR exhibited FRET behaviors indistinguishable from those observed in the absence of the G_s heterotrimer (Fig. 2b,3b). By contrast, agonist-activated β_2AR complexes exhibited a distinct low-FRET (~0.4) state with similar FWHM values (~0.14) (Fig. 3b). This low-FRET value reflects an inter-dye distance of approximately 55Å (Extended Data Fig. 2e), in close agreement with molecular dynamics simulations of the β_2AR-G_s complex (Extended Data Fig. 5a–c). Analogous low-FRET states were observed when agonist-activated receptor was immobilized *via* a biotinylated G_s heterotrimer (Extended Data Fig. 6a–d). The proportion of receptors exhibiting low FRET (Fig. 3b), as well as the fraction of time individual receptors occupied low-FRET states (Extended Data Fig. 7a), correlated with ligand efficacy (Fig. 1b). Consistent with the known basal activity of β_2AR[17], low levels (5–20%) of G_s coupling were evidenced in the absence of ligand and in the presence of alp (Fig. 3b; Extended Data Fig. 7a).

To examine the role of ligand efficacy on the rates of β_2AR-G_s complex formation, M1-immobilized β_2AR (Fig. 3c) was imaged in the presence of 30 μM GDP at increasing G_s concentrations, where reversible transitions between high- and low-FRET states could be quantified using a two-state hidden Markov Model (HMM) (Fig. 3d; **Methods**). Consistent with a bimolecular reaction entailing at least one ligand-dependent, rate-determining process that precedes complete G_s coupling, we found that rates of low-FRET state formation increased with G_s concentration and then plateaued (Fig. 3e; Extended Data Table 1).

Based on the initial slope of the G_s-dependent increase in the rate of low-FRET state formation, we estimate the apparent G_s on rate to β_2AR at ~0.03 and ~0.05 $\mu M^{-1}s^{-1}$ for clen and epi, respectively (Fig. 3e; Extended Data Table 1). These rates are orders of magnitude slower than expected for the binding of large entities[18]. They are, however, similar to bioluminescence resonance energy transfer measurements of β_2AR-mediated G_s activation in living cells (ca. 2–3 s^{-1})[19], where G_s lipidation localizes the heterotrimer to cellular membranes. They are also consistent with the observation that rate-limiting conformational

changes within the rhodopsin-G_t complex precede GTP loading, although G_t activation occurs at a faster rate[20]. Hence, either initial interactions between G_s and β_2AR preceding low-FRET state formation are highly transient (≪100ms) or do not immediately precipitate a FRET change. We therefore hypothesized that G_s coupling may be rate-limited by one or more ligand-dependent conformational processes that occur within a high-FRET β_2AR-G_s complex.

Ligand impacts on β_2AR-G_s stability

To examine the stability of apyrase-treated β_2AR-G_s complexes in the presence of partial and full agonists, we measured the dissociation rate of β_2AR from immobilized G_s heterotrimers (Extended Data Fig. 6a). Under low illumination intensity, where photobleaching was negligible, immobilized β_2AR-G_s complexes exhibited lifetimes of 5–10 minutes (Extended Data Table 2). Notably, these lifetimes decreased ~20–100 fold in the presence of physiological concentrations of GDP (30 μM) or GTP (100 μM)[21] (Extended Data Table 2), to become similar to those observed in cell-based studies of β_2AR-G_s[19] and β_1AR-G_s complexes[22]. Hence, β_2AR-G_s complexes generally persist for multiple seconds in the presence of nucleotide and dissociate approximately two-fold faster in the presence of GTP compared to GDP. These observations are consistent with specific interactions between the receptor and nucleotide-bound G protein and suggest nucleotide-specific dissociation pathways.

To track changes in FRET efficiency within the nucleotide-depleted β_2AR-G_s complex upon GDP or GTP nucleotide binding, we performed analogous experiments at high spatial and temporal resolution (Fig. 4; Extended Data Fig. 6a,e,f). In contrast to the relatively slow rates of complex dissociation, the rapid introduction (ca. 100 ms mixing time) of either GDP (30 μM) or GTP (100 μM) gave rise to an immediate increase, or broadening, of the low-FRET state (ΔFRET ~0.05–0.1) (Fig. 4; Extended Data Fig. 6e,f). These data indicate that nucleotides bind the nucleotide-free β_2AR-G_s complex at, or near, the diffusion limit, and that binding results in structural and/or dynamic changes in TM6 that initiate its return towards the helix bundle. Strikingly, these rapid changes were followed by formation of a relatively long-lived, predominantly high-FRET configuration from which reversible transitions to lower-FRET states occurred with frequencies and durations that were efficacy dependent (Fig. 4; Extended Data Fig. 6e,f).

The addition of GTP triggered transitions to high-FRET that were more rapid and complete than observed for GDP, and both the rate and efficiency of high-FRET state formation were greater for full agonists than for partial agonists (Fig. 4b,d; Extended Data Fig. 6f). These findings provide direct evidence for nucleotide-specific dissociation pathways, and suggest that β_2AR-G_s(GNP) complexes can access multiple conformations distinct from the nucleotide-free state observed crystallographically[6]. The observed persistence of high-FRET, GDP- and GTP-loaded configurations implies the existence of relatively long-lived, β_2AR-G_s(GDP) complexes during initial binding that precede low-FRET state formation, as well as long-lived β_2AR-G_s(GTP) complexes after G protein activation. While the absolute rates we observe may be influenced by interactions between the lipid modifications on G_s and the detergent micelle surrounding β_2AR, pre- and post-coupled GEF-G protein

complexes have been evidenced in distinct systems using independent methods[23–26] and may have important consequences for GPCR signaling.

Ligand impact on G protein activation

The effect of ligand efficacy on the allosteric link between β_2AR and G_s, and its role in nucleotide exchange was further examined in steady-state experiments using M1-immobilized receptor in the presence of activating ligands, nucleotide, and 8μM G_s (Fig. 5a; Extended Data Fig. 7b,c). Under such conditions, G_s dissociation events are expected to be slow (ca. ~0.1–0.2 s^{-1}; Extended Data Table 2), while dynamic processes within the β_2AR-G_s complex should occur rapidly (Fig. 4). As noted above, β_2AR-G_s complexes can exhibit three distinct FRET states: (1) a low-FRET, nucleotide-free state (0.4); (2) a high-FRET, agonist- (0.64) or partial agonist- (0.72) bound state while the receptor remains associated with G_s; and (3) an intermediate-FRET state (~0.5) reflecting a GDP-bound β_2AR-G_s complex with a distinct mode of interaction between TM6 and the α5-helix that is relatively short lived (Fig. 4c). Because the two lower-FRET states can be seen clearly only in pre-steady-state experiments, we analyzed our steady state data as a two-state system where states 1 and 3 are collapsed into a single, broadly defined (~0.4–0.5) low-FRET state.

To learn about the rate-limiting features of β_2AR-G_s complex formation, we examined the rates of low- and high-FRET state formation ($k_{high\rightarrow low}$; $k_{low\rightarrow high}$, respectively) over a range of GDP concentrations. As expected for binding of a GDP-bound G_s heterotrimer, $k_{high\rightarrow low}$ was largely independent of GDP concentration for all agonists (Extended Data Fig. 8a). By contrast, $k_{low\rightarrow high}$ increased with GDP and plateaued at concentrations above ~20 μM (Fig. 5a). Consistent with TM6 dynamics occurring within the β_2AR-G_s complex, the maximum rates exiting low FRET were ~5–15-fold more rapid than the apparent G_s dissociation rate (Extended Data Table 2). The rank order of the low- to high-FRET state transition was: clen> salb>salm>BI>iso>epi. Given that GDP binding to the nucleotide-free β_2AR-G_s complex is rapid (Fig. 4a,c; Extended Data Fig. 6e), we conclude that the transition out of low-FRET states into high FRET is rate-limited by one or more ligand-dependent processes within the β_2AR-G_s (GDP) complex.

As low FRET includes both nucleotide-free and GDP-bound complexes (Fig. 4a,c), we speculated that the slower rates of return to high FRET observed for full agonists (Fig. 5a) may reflect higher proportions of the relatively stable nucleotide-free state. We therefore undertook an evaluation of differences in the proportion of nucleotide-free β_2AR-G_s complexes in the presence of distinct agonists using the experimentally observed mean value of the low-FRET state as a function of GDP concentration (Fig. 5b,c). This analysis revealed that the low-FRET state values observed at saturating GDP concentration (100 μM) were considerably lower for full agonists compared to partial agonists, more closely approximating the FRET value (~0.4) observed for the nucleotide-free β_2AR-G_s complex (Extended Data Fig. 8c,d). Consistent with GDP binding promoting return to high FRET, increasing GDP concentrations increased the mean values of the low-FRET states, while decreasing their time-averaged occupancies (Fig. 5b,c). The concentration dependence of these effects revealed that full agonists exhibited EC_{50} values that were approximately 2–3-fold higher than for partial agonists (Fig. 5d; Extended Data Fig. 8e). These data suggest that

β_2AR-G_s complexes exhibit higher affinity for GDP when bound to partial agonists compared to full agonists. They also support the notion that low-FRET states represent a mixture of nucleotide-free and GDP-bound β_2AR-G_s configurations, where complexes activated by full agonists spend more time on average in the relatively stable, nucleotide-free state. These findings may help explain why epi promotes a greater extent of [^{3}H]GDP release from β_2AR compared to salb[27], despite both agonists promoting low FRET states at similar rates (Fig. 3e). As the rates of GDP binding to nucleotide-free β_2AR-G_s complexes are rapid, and appear indistinguishable at the present time resolution (Fig. 4a,c), we conclude that more efficacious agonists increase the probability of GDP release and thus the likelihood that nucleotide-free states are achieved.

To test this model directly, we performed analogous GTP titrations in the presence of a fixed, saturating GDP concentration (30 μM) (Extended Data Fig. 7b,c). As anticipated, the transition rate from low-to-high FRET ($k_{low \rightarrow high}$) was in all cases specifically increased at even the lowest GTP concentrations tested (100nM) (Fig. 5e; Extended Data Fig. 8b). While the absolute values of $k_{low \rightarrow high}$ were greater for partial agonists in the presence of GTP (Fig. 5e), the fold increase in rate, and hence the magnitude reduction in low-FRET state lifetime, correlated with ligand efficacy in the order: epi>iso>BI>salm>salb>clen (Fig. 5e,f; Extended Data Fig. 8h). Taken together with the rapid rates of GDP and GTP binding to nucleotide-free β_2AR-G_s complexes (Fig. 4), we conclude that the relatively short-lived, active-like, low-FRET β_2AR conformations evidenced in the presence of partial agonists (Fig. 5a,e,f) predominantly reflect failed attempts at nucleotide release, and that full agonists more efficiently promote relatively long-lived, nucleotide-free configurations (Extended Data Fig. 8f,g). Hence, ligands with greater efficacy preferentially promote GDP release, and under competitive conditions, rapid and efficient GTP loading to the subpopulation of nucleotide-free complexes. The more rapid return of β_2AR-G_s(GTP) complexes to high-FRET states following GTP loading argues that the terminal phosphate of GTP lowers the barrier for the rate-limiting conformational transition that enables the return of TM6 to its position adjacent to the helix bundle. This distinction may reflect GTP-specific impacts on G_s heterotrimer stability.

DISCUSSION

We have examined ligand-activated G_s binding, nucleotide exchange, and G_s release, from the perspective of time-dependent changes in β_2AR conformation. The results illuminate the established concept of ligand efficacy in terms of a specific kinetic framework for the activation pathway (Fig. 6a). Quantifying the ligand-dependence of both the rate and the efficiency of G_s coupling in the presence of physiological GDP concentrations revealed that the process is achieved by rate-limiting conformational processes intrinsic to the β_2AR-G_s complex (Fig. 3e). Although the nature of the interactions preceding excursions to low-FRET, active-like conformations are not presently known, the rates evidenced at saturating G_s concentration (Fig. 3e) suggest ligand-specific impacts on the probability that $G\alpha_s$ productively engages the intracellular face of β_2AR after the complex has formed (Fig. 6a). The molecular events underpinning these early activation steps minimally include the remodeling of the $\beta6\alpha5$ loop proximal to the $G\alpha_s$ switch regions, and translation and

rotation of the α5 helix of G_α away from the GDP binding pocket towards the intracellular vestibule in β_2AR created by the outward movement of TM6[28–35] (Fig. 6b).

The apparent differences in initial engagement and the rate-limiting conformational changes leading to active-like, lower-FRET states (Fig. 3e; Extended Data Table 1), provide an estimate of the relative ligand-dependent efficiencies (η_1) in these hidden early steps (**Methods**). A second determinant of ligand efficacy (η_2) – which likely arises from differences in how efficiently the α5 helix C-terminus of $G\alpha_s$ productively engages, and forms stabilizing interactions, with the intracellular β_2AR surface[34] – can be estimated from the propensity of full agonists to more effectively promote GDP release (**Methods**). Using the normalized parameters ($\boldsymbol{\eta_1}$, $\boldsymbol{\eta_2}$), the efficacies of activating ligands relative to epi ($\boldsymbol{\varepsilon}$) can be ranked in terms of their effective rates of generating G_s(GTP) from G_s(GDP) (Fig. 6c; **Methods**). In doing so, we estimate that iso is ~8-times more efficacious than clen. While these predictions suggest greater efficacy differences than inferred from *in vitro* GTP turnover assays (Fig. 1b), they are in close agreement with cyclic AMP production in living cells (Fig. 6d). Ligand-specific disparities in our calculated values versus the measured ligand efficacy values may reflect agonist-specific differences in GTP binding rates and/or affinities, which could not be accurately quantified.

In addition to providing quantitative insights into ligand efficacy, the present smFRET studies shed light on β_2AR-G_s conformations that are structurally distinct from the nucleotide-free complex (Fig. 1a). While GDP- and GTP-bound complexes may be too unstable for crystallographic study, in-depth characterizations of these states are expected to provide important insights into both G protein coupling rates and specificities. Quantitative single-molecule imaging investigations will be critical in such efforts, as well as for delineating distinct ligand-dependent GPCR signaling pathways.

Extended Data

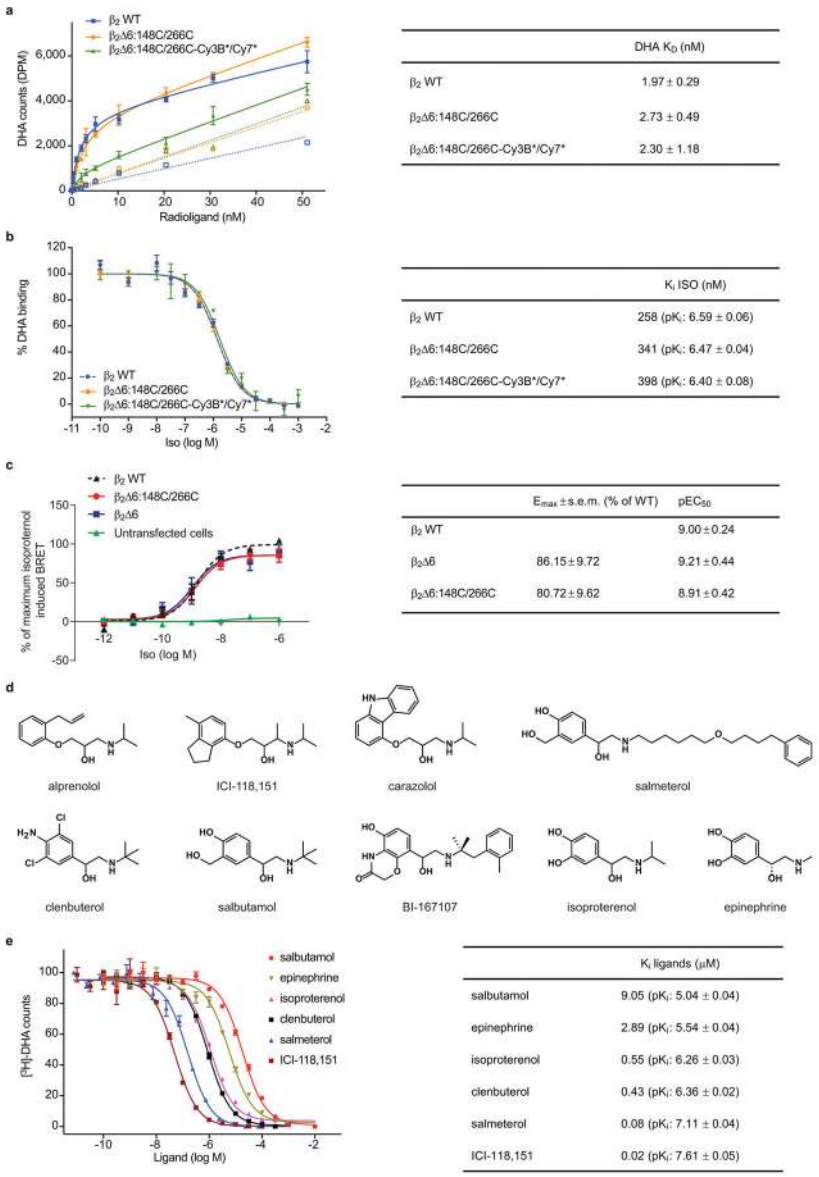

	DHA K_D (nM)
β_2 WT	1.97 ± 0.29
$\beta_2\Delta6$:148C/266C	2.73 ± 0.49
$\beta_2\Delta6$:148C/266C-Cy3B*/Cy7*	2.30 ± 1.18

	K_i ISO (nM)
β_2 WT	258 (pK_i: 6.59 ± 0.06)
$\beta_2\Delta6$:148C/266C	341 (pK_i: 6.47 ± 0.04)
$\beta_2\Delta6$:148C/266C-Cy3B*/Cy7*	398 (pK_i: 6.40 ± 0.08)

	E_{max} ± s.e.m. (% of WT)	pEC_{50}
β_2 WT		9.00 ± 0.24
$\beta_2\Delta6$	86.15 ± 9.72	9.21 ± 0.44
$\beta_2\Delta6$:148C/266C	80.72 ± 9.62	8.91 ± 0.42

	K_i ligands (μM)
salbutamol	9.05 (pK_i: 5.04 ± 0.04)
epinephrine	2.89 (pK_i: 5.54 ± 0.04)
isoproterenol	0.55 (pK_i: 6.26 ± 0.03)
clenbuterol	0.43 (pK_i: 6.36 ± 0.02)
salmeterol	0.08 (pK_i: 7.11 ± 0.04)
ICI-118,151	0.02 (pK_i: 7.61 ± 0.05)

Extended Data Figure 1.

Ligand binding properties of $\beta_2\Delta6$-148C/266C. **a,** [^{3}H]-dihydroalprenolol (DHA) saturation binding on purified β_2AR, comparing wild-type (WT; blue squares) versus unlabeled (orange circles) and labeled (green triangles) $\beta_2\Delta6$-148C/266C. Affinities (K_d) are shown in the table. Non-specific binding controls are shown as corresponding open symbols. Error bars represent the standard error of the mean (s.e.m.) from triplicate measurements. **b,** [^{3}H]-DHA–iso competition binding on purified β_2AR, comparing wild-type (WT; blue circles) versus unlabeled (orange squares) and labeled (green triangles) $\beta_2\Delta6$-148C/266C. Affinities (K_i) are reported in the table. Error bars represent the s.e.m. from triplicate measurements. **c,** Dose-response curves of the BRET-based cAMP biosensor CAMYEL with wild-type (WT) β_2AR (black triangles) and the mutants $\beta_2\Delta6$ (blue squares) and $\beta_2\Delta6$-148C/266C (red

circles). Data from untransfected cells are shown in green triangles. Data from five independent experiments were normalized to the maximal isoproterenol response by WT β_2AR in each experiment and globally fit to the entire data set, with the error bars representing the s.e.m., as reported in the table. **d,** Skeletal structures of ligands used in the current study. **e,** [^{3}H]-DHA competition binding on unlabeled $\beta_2\Delta$6-148C/266C for ligands used in the current study, except for cz and BI, for which the ultra-high affinities reported (32 pM and 84 pM, respectively) would not allow us to determine them accurately in our assay. Instead, we used concentrations of 1 μM for both in all our measurements. The calculated K_is are shown on the table.

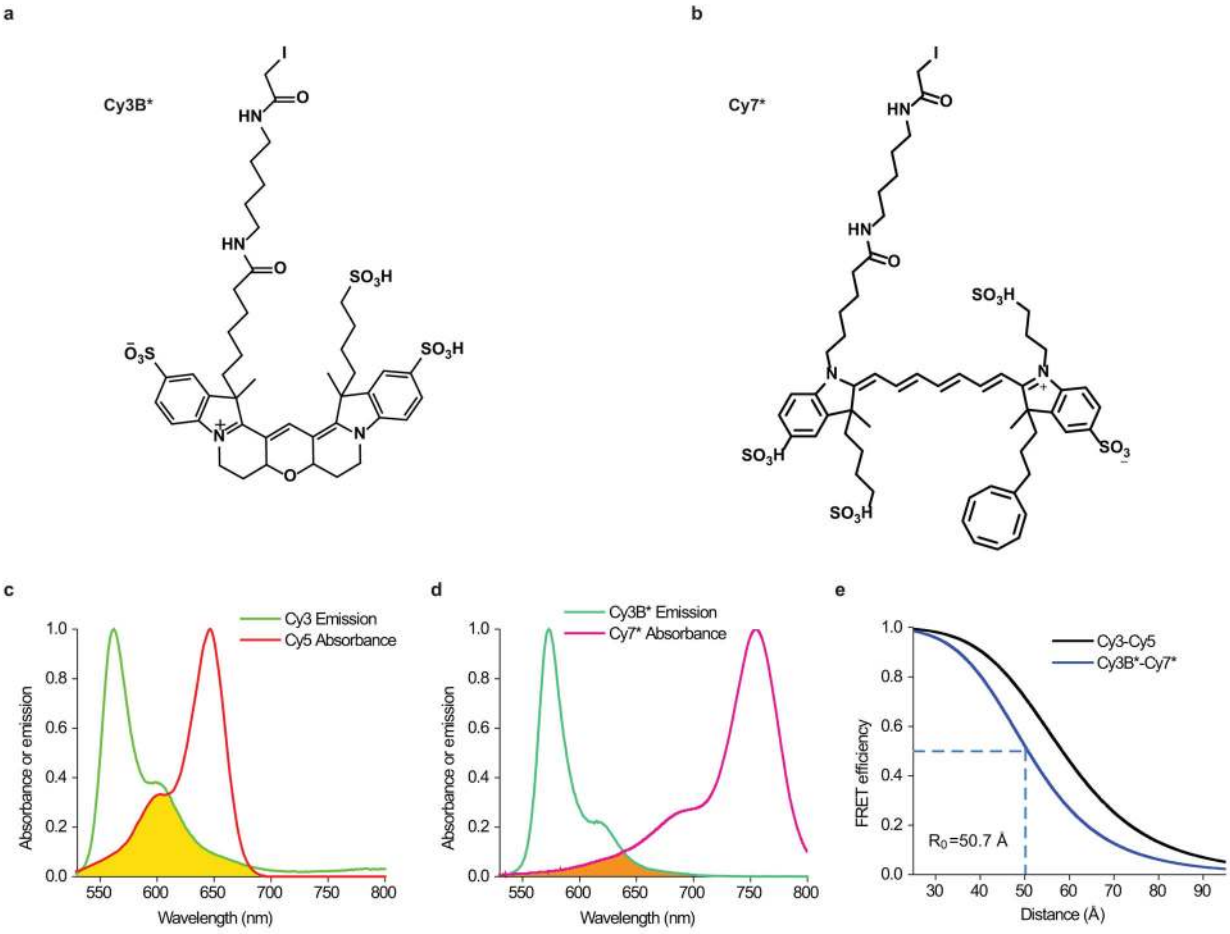

f

	Anisotropy	S1_hh	S1_hv	S1_vh	S1_vv	G Factor	Trials	Std. Err. Anisotropy (%)
free dye	0.04614	0.73E+06	0.32E+06	0.28E+06	0.14E+06	0.44422	10	4.48
apo	0.2093	3.00E+06	1.44E+06	1.29E+06	1.12E+06	0.48166	3	0.754
iso	0.2101	2.96E+06	1.42E+06	1.27E+06	1.11E+06	0.47949	10	2.22
BI	0.2119	2.93E+06	1.42E+06	1.26E+06	1.10E+06	0.48549	10	2.99
BI + G_s	0.2240	2.83E+06	1.36E+06	1.21E+06	1.08E+06	0.48069	10	2.15

Extended Data Figure 2.

Fluorophore structures and properties. **a–b,** Skeletal structures of the modified Cy3B* donor (**a**) and Cy7* acceptor (**b**) fluorophores. **c–d**, Normalized donor fluorophore emission (Cy3: green; Cy3B*: dark green) and acceptor fluorophore absorbance (Cy5: red; Cy7*: dark magenta) spectra for Cy3/Cy5 (**c**) and Cy3B*/Cy7* (**d**) FRET pairs. The spectral overlap integral (shaded region) was calculated and used to determine the Förster distance (R_0) values for each pair. **e,** Inter-dye FRET efficiencies of the Cy3/Cy5 (black) and Cy3B*/Cy7* (blue) donor and acceptor fluorophore pairs as a function of inter-dye distances calculated based on R_0 values. **f,** Bulk anisotropy measurements on Cy3B*-labeled $\beta_2\Delta$6-148C/266C.

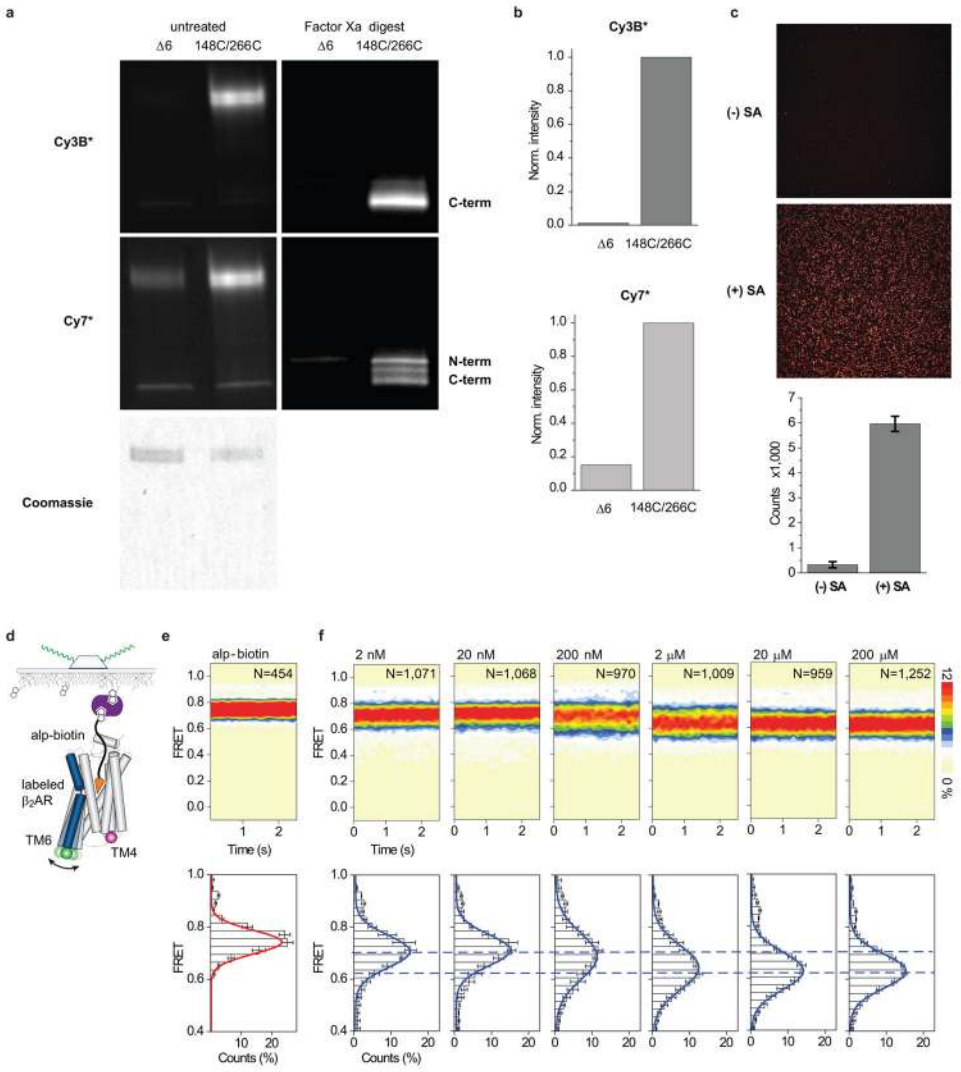

Extended Data Figure 3.

smFRET experimental controls. **a,** Site-specific labeling. SDS-PAGE gels under green (540 nm) or near IR (740 nm) epi-illumination for fluorescence visualization of Cy3B* or Cy7* labeling of $\beta_2\Delta6$ and $\beta_2\Delta6$-148C/266C. Coomassie-stained gel image is shown as a gel-loading control. Digestion with Factor Xa protease and deglycosylation with PNGase F leads to separation of the 148C and 266C labeling sites on generated N-terminal and C-terminal fragments, respectively. For gel source data, see Supplementary Figure 1. **b,** Quantification of Cy3B*/Cy7*-labeling specificity of full-length $\beta_2\Delta6$-148C/266C. Data is normalized to $\beta_2\Delta6$-148C/266C labeling. **c,** Specificity of streptavidin-mediated receptor immobilization. Frame capture from immobilization movies showing labeled $\beta_2\Delta6$-148C/266C on streptavidin-free (-SA) or streptavidin-coated (+SA) surfaces. Bar graph shows the number of immobilized, labeled β_2AR in these conditions. Error bars represent the standard deviation from two replicates. **d,** Schematic of labeled β_2AR immobilization *via* biotinylated alp (alp-biotin). **e,** FRET population contour plot and histogram for alp-biotin-immobilized receptor shows correspondence with the FRET population distribution of biotin-M1-Fab-

immobilized, alp-bound, labeled β_2AR (Fig. 2b). Histogram error bars represent the standard deviation from four replicates with N total molecules analyzed. **f,** FRET population contour plots (top row) and histograms (bottom row) for epi titration on biotin-M1-Fab-immobilized, labeled $\beta_2\Delta$6-148C/266C (Fig. 2c). Dashed lines (blue) highlight the mean FRET values for the lowest (2 nM; top dashed line) and highest (200 μM; bottom dashed line) epi concentrations tested. Histogram error bars represent the standard deviation from three replicates with N total molecules analyzed. The scale bar on the right indicates relative populations for the contour plots.

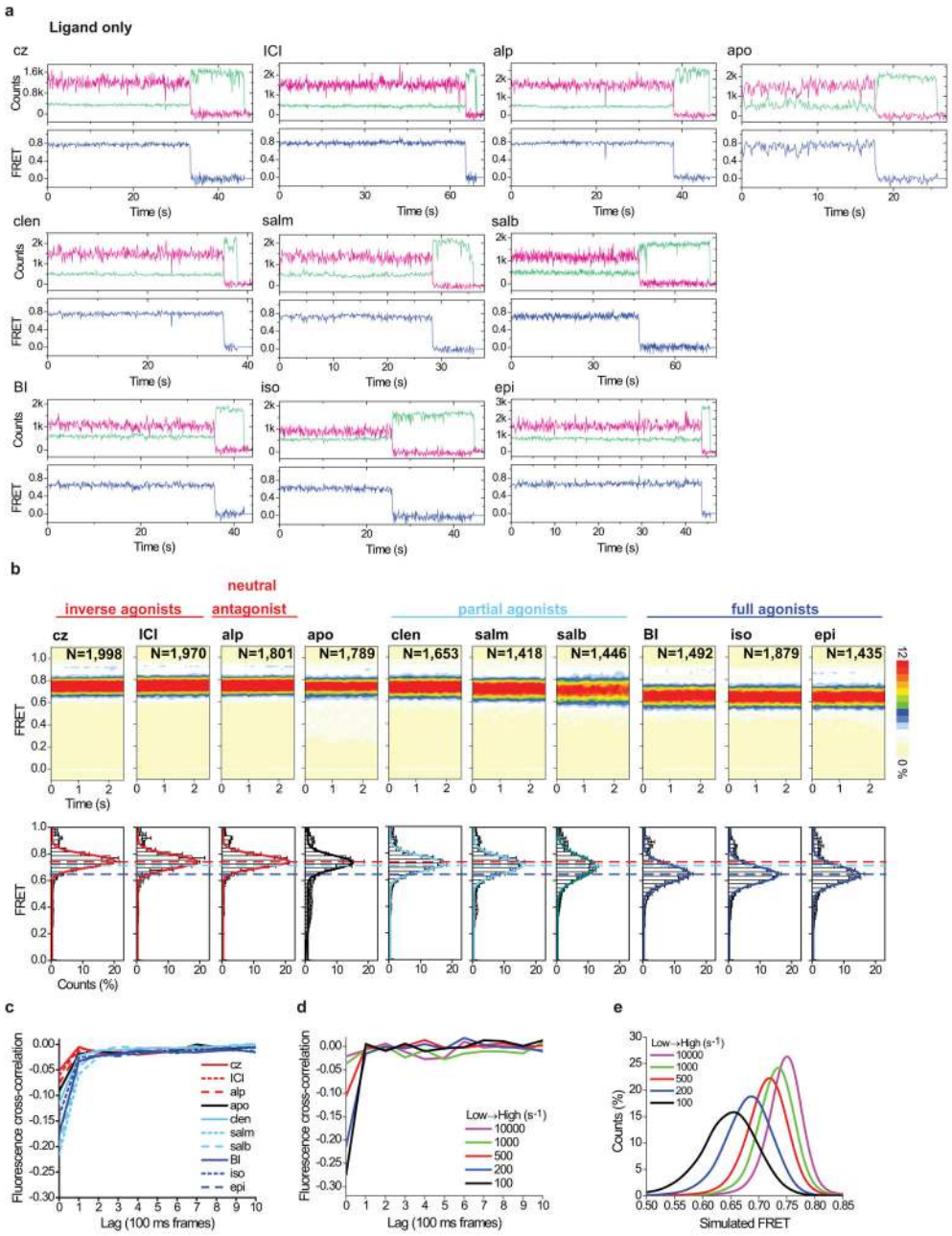

Extended Data Figure 4.

a, Sample fluorescence (green for Cy3B*; magenta for Cy7*) and FRET (blue) time traces for biotin-M1-Fab-immobilized, labeled $\beta_2\Delta$6-148C/266C imaged in the absence and presence of saturating ligands. **b,** Same as Fig. 2b but with the full FRET efficiency range (0–1) shown for the population histograms (bottom row). **c,** Plots showing the mean cross correlation values of donor and acceptor fluorescence as a function of lag time for the ensemble of individual fluorescence traces obtained from experiments shown in Figure 2b. d, Plots showing the mean cross correlation values of donor and acceptor fluorescence as a function of lag time for an ensemble of simulated fluorescence trajectories rapidly fluctuating between high (0.75) and intermediate (0.55) FRET values with varying low- to high-FRET transition rate constants (colored lines), where the high- to low-FRET transition rate is held constant at 100 s^{-1} (**Methods**). **e,** FRET distributions of the simulated data, as described in panel **d**.

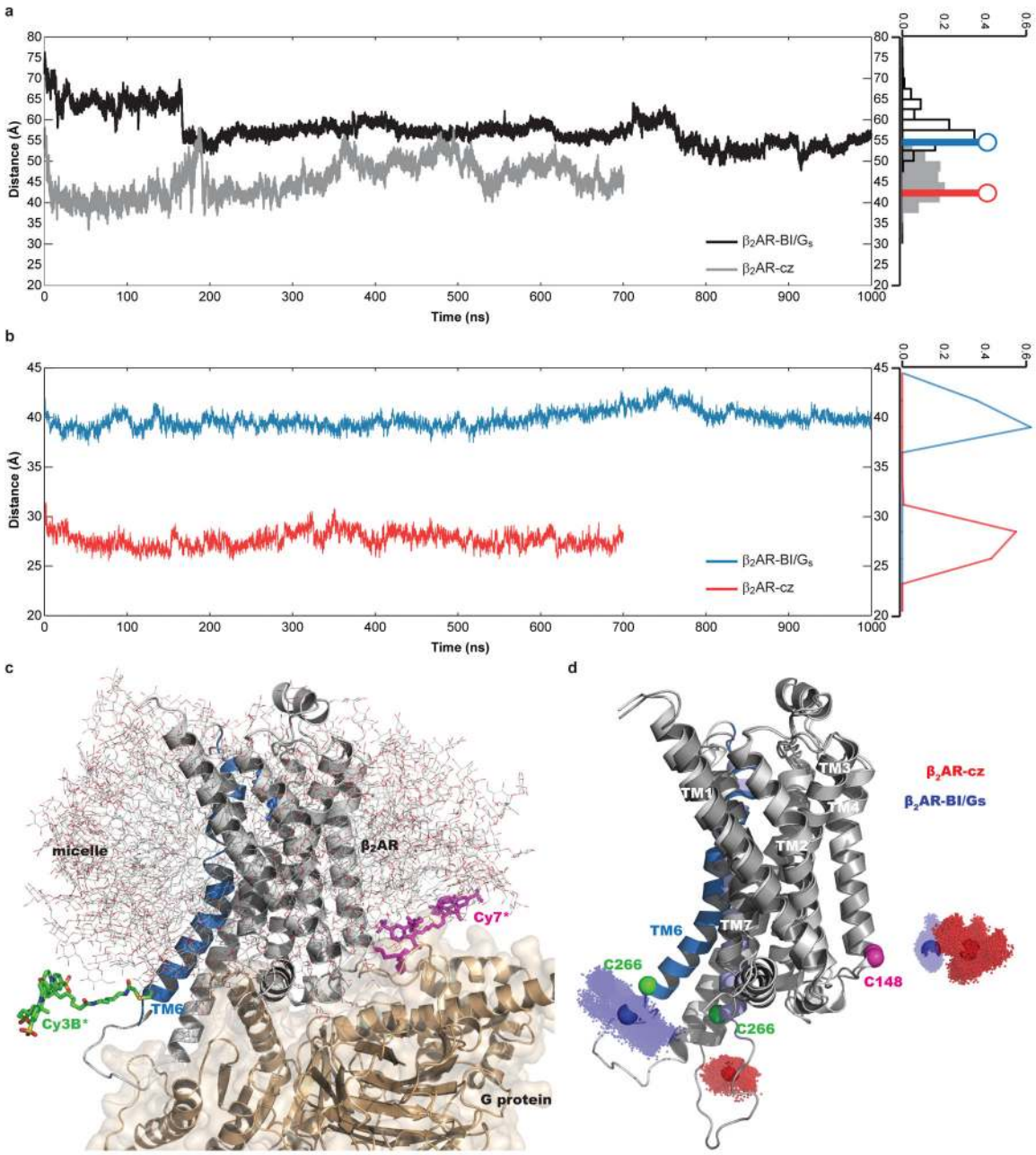

Extended Data Figure 5.

All-atom molecular dynamics simulations of the Cy3B*/Cy7*-labeled β_2AR in a detergent micelle. **a,** Time evolution of the distance between the dyes. Time dependence of the distances between the midpoints of the dyes along the simulation trajectories is shown for the β_2AR-cz (gray) and β_2AR-BI/G_s (black) systems. The distributions are displayed as histograms on the right; gray bars: β_2AR-cz; clear bars: β_2AR-BI/G_s. The estimated inter-dye distances derived from the experimental mean FRET values (Figs. 2b,3b; Extended Data Fig. 2e) are indicated by solid lines topped with circles (β_2AR-cz: red; β_2AR-BI/G_s: blue). **b,** Time evolution of the distance between C_{alpha} carbons at the labeling site. C_{alpha}-C_{alpha}

distances for β_2AR-cz: red and β_2AR-BI/G_s: blue. **c,** The simulated dye-tethered β_2AR-BI/G_s system embedded in a DDM micelle (gray sticks). β_2AR is rendered in gray, with TM6 and the agonist (BI) highlighted in blue. The G_s protein is rendered in wheat color surrounded by its molecular surface to indicate the excluded volume for dye movements. The Cy3B* and Cy7* dyes are colored green and magenta, respectively. Water molecules, ions, and detergent molecules distant from the β_2AR structure are omitted. **d,** Positions explored by the midpoints of the dyes during the simulations are shown as clusters of dots in the context of the β_2AR-cz (transparent red dots) and β_2AR-BI/G_s (transparent blue dots) complexes; the center of mass of each collection of dots is indicated by a solid sphere. C_{alpha} carbons for labeled positions $148^{4.40}$ and $266^{6.28}$, are shown as magenta and green spheres, respectively.

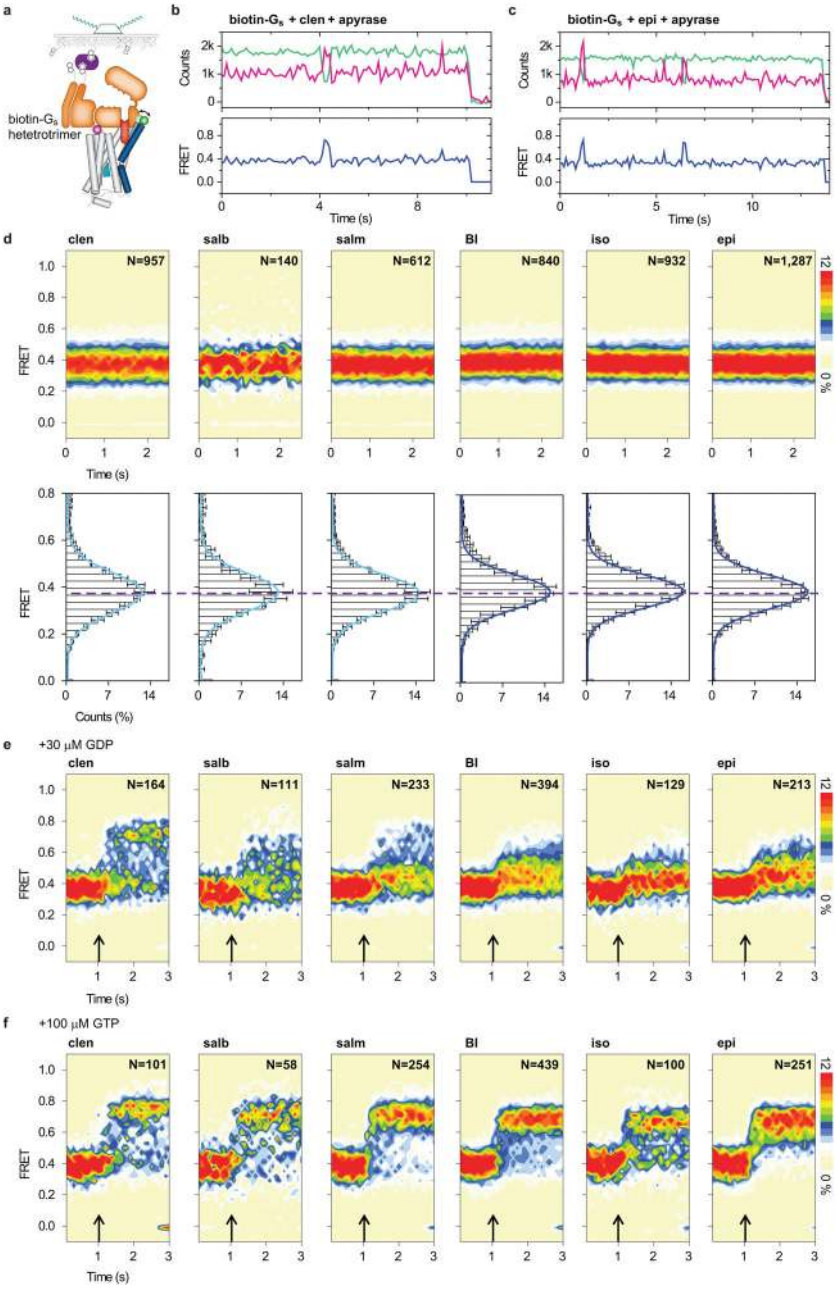

Extended Data Figure 6.

smFRET imaging of biotin-G_s-immobilized, labeled β_2AR. **a,** Schematic of labeled β_2AR immobilization *via* biotinylated G_s heterotrimer. **b–c,** Representative fluorescence (green for Cy3B*; magenta for Cy7*) and FRET (blue) time traces for biotin-G_s-immobilized, labeled $\beta_2\Delta$6-148C/266C imaged in the presence of clen (**b**) or epi (**c**) in nucleotide-free conditions (apyrase-treated). **d,** FRET population contour plots (top row) and histograms (bottom row) for biotin-G_s-immobilized $\beta_2\Delta$6-148C/266C imaged in the presence of partial and full agonists in nucleotide-free conditions. The dashed line indicates the invariant mean FRET value (~0.38) for all agonists tested. Histogram error bars represent the standard deviation

from three replicates with N total molecules analyzed. **e–f,** FRET population contour plots of biotin-G_s-immobilized β_2Δ6-148C/266C in the presence of agonists exhibiting FRET transitions upon rapid addition (arrow) of 30 μM GDP (**e**) or 100 μM GTP (**f**). Scale bar on the right indicates the relative population for the contour plots.

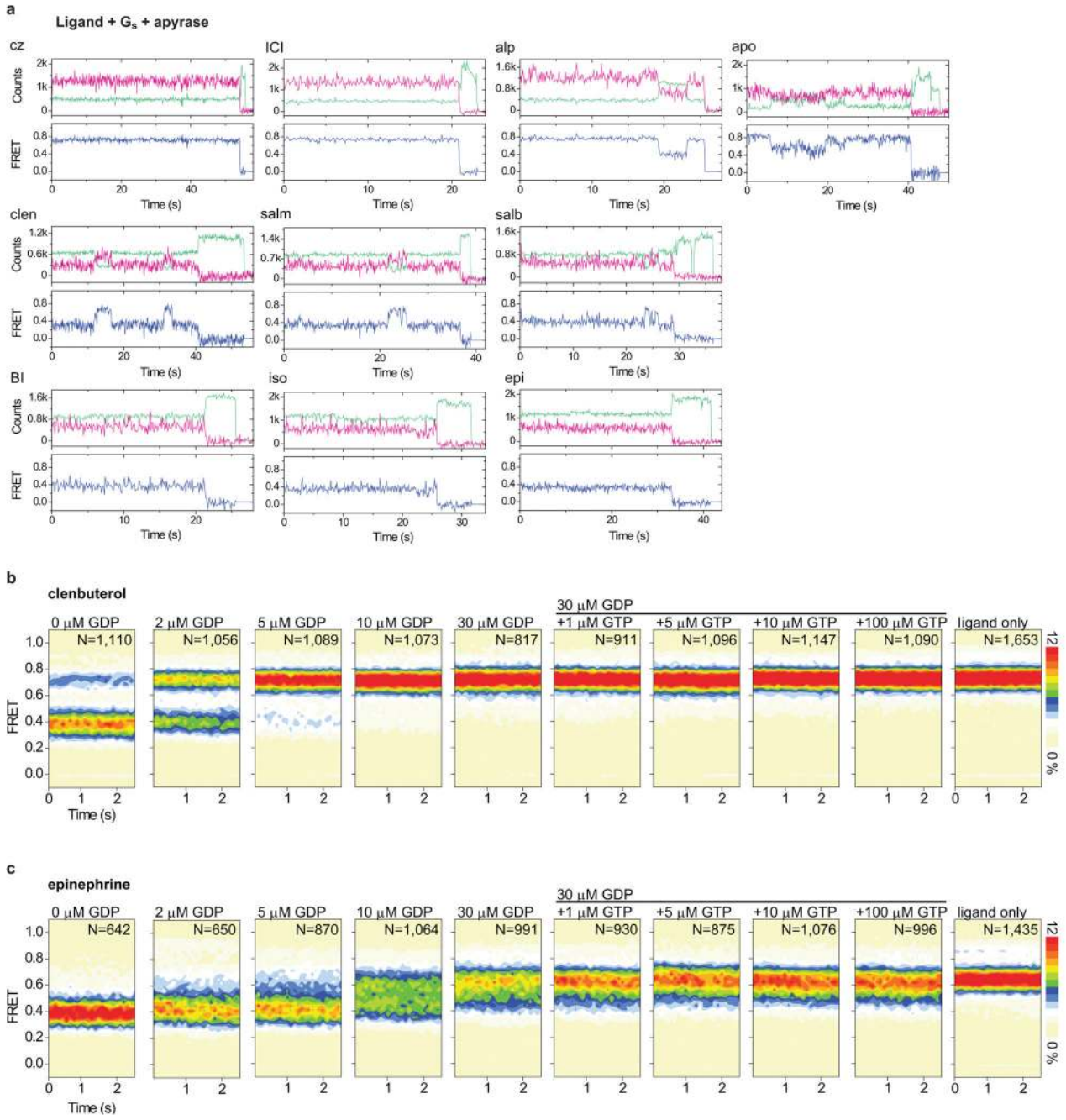

Extended Data Figure 7.

a, Sample fluorescence and FRET time traces for biotin-M1-Fab-immobilized, labeled β_2Δ6-148C/266C imaged in the absence and presence of saturating ligands plus 8 μM G_s in

nucleotide-free (after apyrase treatment) conditions. **b–c,** FRET population contour plots for biotin-M1-Fab-immobilized, labeled β_2Δ6-148C/266C imaged in the presence of the agonists clenbuterol (**b**) or epinephrine (**c**), 8 μM G_s and increasing concentrations of GDP (Fig. 5a) or GTP in the presence of saturating GDP (30 μM) (Fig. 5e) with N indicating the total number of molecules analyzed from two replicates. Nucleotide-free (0 μM GDP; from Fig. 3b) and ligand only (from Fig. 2b) conditions are included as references. Scale bar on the right indicates the relative population for the contour plots.

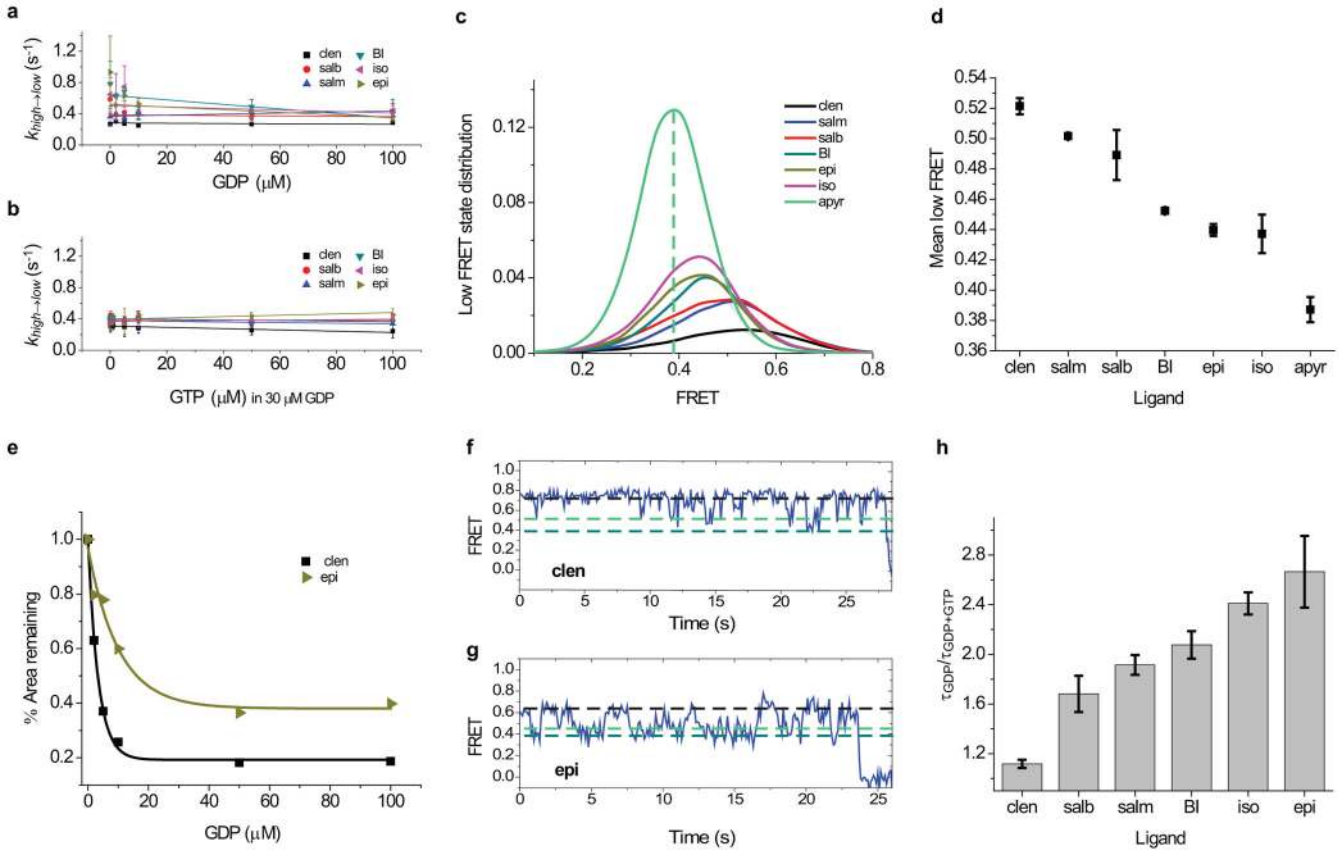

Extended Data Figure 8.

a–b, Transition rates from high- to low-FRET states ($k_{high\rightarrow low}$) of labeled β_2AR with different agonists, saturating G_s (8 μM) and increasing GDP concentrations (2–100 μM)(**a**) or increasing GTP concentrations (0–100 μM) in 30 μM GDP (**b**). **c,** Low-FRET state distributions for labeled β_2AR with different agonists in 100 μM GDP and saturating G_s showing their overlap with the distribution in the presence of epi and saturating G_s in nucleotide-free conditions (apyr) (Fig. 3b). The dashed line shows the mean FRET value for apyr. **d,** Mean low FRET values from **c. e,** The percent change in the area of the low-FRET state population distributions for clen (black squares) and epi (dark yellow triangles)(as shown in Fig. 5b and c, respectively) was plotted with increasing GDP concentration (0–100 μM) and fitted to a single exponential decay function to derive the GDP EC_{50}. **f–g,** Sample FRET traces (blue line) of labeled β_2AR in the presence of clen (**f**) or epi (**g**) plus 100 μM GDP and saturating G_s. Dashed lines indicate each ligand's corresponding mean high FRET

value (black), mean low FRET value (light green) and mean FRET value in nucleotide-free conditions (dark green). **h,** The ratio of the low-FRET state lifetime of β_2AR in the presence of saturating G_s and GDP (τ_{GDP}) over the low-FRET state lifetime in saturating GTP plus 30 μM GDP ($\tau_{GDP+GTP}$)(Fig. 5f) is shown for different agonists. All error bars in the figure represent the standard deviation from two replicates.

Extended Data Table 1

Apparent on rate and transition rates from high- to low-FRET states calculated from the data presented in Fig. 3e.

	apparent k_{on} ($\mu M^{-1}s^{-1}$)	$k_{high \rightarrow low}$ (s^{-1})
alp	$\ll$0.02	-
clen	0.03	0.4
salm	0.04	0.6
salb	0.04	0.7
BI	0.04	0.7
epi	0.05	0.7
iso	0.04	1.1

Extended Data Table 2

Lifetimes of biotin-G_s-immobilized β_2AR in the nucleotide-free state and upon addition of GDP or GTP and the lifetimes of biotin-M1-Fab-immobilized β_2AR in the absence of G_s.

Ligand	Lifetime			
	M1-immobilized (min)	Biotin-G_s-immobilized		
		GNP-free (min)	+GDP (s)	+GTP (s)
clen	14.4 ± 2.1	8.3 ± 1.3	9.8 ± 1.6	6.8 ± 0.5
salb	18.1 ± 8.4	5.0 ± 0.4	8.2 ± 0.9	6.4 ± 0.1
salm	10.8 ± 4.1	3.5 ± 1.6	9.0 ± 0.4	6.6 ± 0.2
BI	11.0 ± 5.5	8.0 ± 3.2	9.4 ± 0.6	6.2 ± 0.1
iso	12.7 ± 3.1	6.0 ± 5.2	9.8 ± 1.3	5.8 ± 0.1
epi	13.2 ± 3.4	11.2 ± 5.1	11.8 ± 1.2	6.4 ± 0.1

Supplementary Material

Refer to Web version on PubMed Central for supplementary material.

Acknowledgments

We thank Dr. Mark Howarth for the kind gift of trans-divalent streptavidin, and Chaya Stern in the lab of Prof. John Chodera at MSKCC for constructing the CHARMM-consistent parameters for the dyes used in the MD simulations. Computational resources are gratefully acknowledged: an XSEDE allocation at the Texas Advanced Computing Center at the University of Texas at Austin (Stampede supercomputer, project TG MCB120008), support from resources at the Oak Ridge Leadership Computing Facility (ALCC allocation BIP109) at the Oak Ridge National Laboratory that is supported by the Office of Science of the U.S. Department of Energy under Contract No. DE-AC05-00OR22725; and the resources of the David A. Cofrin Center for Biomedical Information in the HRH Prince Alwaleed Bin Talal Bin Abdulaziz Alsaud Institute for Computational Biomedicine at Weill Cornell Medicine. This work was supported in part by National Institutes of Health Grants GM098859 (S.C.B), R21DA0354585 (J.A.J.,

S.C.B. and G.G.G.), K05DA022413 and R01 MH54137 (J.A.J.), R01GM083118 and R01NS028471 (B.K.K.), and U54GM087519 (H.W. and J.M.P-A.), the German Academic Exchange Service (DAAD) (D.H.), the American Heart Association Postdoctoral fellowship (15POST22700020) (M.M.), and the Novo Nordisk Foundation Center for Basic Metabolic Research (M.H.).

References

1. Pierce KL, Premont RT, Lefkowitz RJ. Seven-transmembrane receptors. Nat Rev Mol Cell Biol. 2002; 3:639–650. [PubMed: 12209124]
2. Vilardaga JP, et al. GPCR and G proteins: drug efficacy and activation in live cells. Mol Endocrinol. 2009; 23:590–599. [PubMed: 19196832]
3. Kenakin T. New concepts in pharmacological efficacy at 7TM receptors: IUPHAR review 2. Br J Pharmacol. 2013; 168:554–575. [PubMed: 22994528]
4. Manglik A, Kobilka B. The role of protein dynamics in GPCR function: insights from the beta2AR and rhodopsin. Curr Opin Cell Biol. 2014; 27:136–143. [PubMed: 24534489]
5. Baker JG. The selectivity of beta-adrenoceptor agonists at human beta1-, beta2- and beta3-adrenoceptors. Br J Pharmacol. 2010; 160:1048–1061. [PubMed: 20590599]
6. Rasmussen SG, et al. Crystal structure of the beta2 adrenergic receptor-Gs protein complex. Nature. 2011; 477:549–555. [PubMed: 21772288]
7. Kruse AC, et al. Activation and allosteric modulation of a muscarinic acetylcholine receptor. Nature. 2013; 504:101–106. [PubMed: 24256733]
8. Huang W, et al. Structural insights into micro-opioid receptor activation. Nature. 2015; 524:315–321. [PubMed: 26245379]
9. Carpenter B, Nehme R, Warne T, Leslie AG, Tate CG. Structure of the adenosine A2A receptor bound to an engineered G protein. Nature. 2016; 536:104–107. [PubMed: 27462812]
10. Yao XJ, et al. The effect of ligand efficacy on the formation and stability of a GPCR-G protein complex. Proc Natl Acad Sci U S A. 2009; 106:9501–9506. [PubMed: 19470481]
11. Manglik A, et al. Structural Insights into the Dynamic Process of beta2-Adrenergic Receptor Signaling. Cell. 2015; 161:1101–1111. [PubMed: 25981665]
12. Nygaard R, et al. The dynamic process of beta(2)-adrenergic receptor activation. Cell. 2013; 152:532–542. [PubMed: 23374348]
13. Cooper M, et al. Cy3B: improving the performance of cyanine dyes. J Fluoresc. 2004; 14:145–150. [PubMed: 15615040]
14. Vafabakhsh R, Levitz J, Isacoff EY. Conformational dynamics of a class C G-protein-coupled receptor. Nature. 2015; 524:497–501. [PubMed: 26258295]
15. Kim HD, et al. Mg2+-dependent conformational change of RNA studied by fluorescence correlation and FRET on immobilized single molecules. Proc Natl Acad Sci U S A. 2002; 99:4284–4289. [PubMed: 11929999]
16. Lamichhane R, et al. Single-molecule view of basal activity and activation mechanisms of the G protein-coupled receptor beta2AR. Proc Natl Acad Sci U S A. 2015; 112:14254–14259. [PubMed: 26578769]
17. Bond RA, et al. Physiological effects of inverse agonists in transgenic mice with myocardial overexpression of the beta 2-adrenoceptor. Nature. 1995; 374:272–276. [PubMed: 7885448]
18. Ferguson A, et al. Functional Dynamics within the Human Ribosome Regulate the Rate of Active Protein Synthesis. Mol Cell. 2015; 60:475–486. [PubMed: 26593721]
19. Gales C, et al. Real-time monitoring of receptor and G-protein interactions in living cells. Nat Methods. 2005; 2:177–184. [PubMed: 15782186]
20. Ernst OP, Gramse V, Kolbe M, Hofmann KP, Heck M. Monomeric G protein-coupled receptor rhodopsin in solution activates its G protein transducin at the diffusion limit. Proc Natl Acad Sci U S A. 2007; 104:10859–10864. [PubMed: 17578920]
21. Traut TW. Physiological concentrations of purines and pyrimidines. Mol Cell Biochem. 1994; 140:1–22. [PubMed: 7877593]
22. Hein P, et al. Gs activation is time-limiting in initiating receptor-mediated signaling. J Biol Chem. 2006; 281:33345–33351. [PubMed: 16963443]

23. Gales C, et al. Probing the activation-promoted structural rearrangements in preassembled receptor-G protein complexes. Nat Struct Mol Biol. 2006; 13:778–786. [PubMed: 16906158]
24. Qin K, Dong C, Wu G, Lambert NA. Inactive-state preassembly of G(q)-coupled receptors and G(q) heterotrimers. Nat Chem Biol. 2011; 7:740–747. [PubMed: 21873996]
25. Westfield GH, et al. Structural flexibility of the G alpha s alpha-helical domain in the beta2-adrenoceptor Gs complex. Proc Natl Acad Sci U S A. 2011; 108:16086–16091. [PubMed: 21914848]
26. Damian M, et al. Ghrelin receptor conformational dynamics regulate the transition from a preassembled to an active receptor:Gq complex. Proc Natl Acad Sci U S A. 2015; 112:1601–1606. [PubMed: 25605885]
27. Murayama T, Ui M. [3H]GDP release from rat and hamster adipocyte membranes independently linked to receptors involved in activation or inhibition of adenylate cyclase. Differential susceptibility to two bacterial toxins. J Biol Chem. 1984; 259:761–769. [PubMed: 6319385]
28. Ceruso MA, Periole X, Weinstein H. Molecular dynamics simulations of transducin: interdomain and front to back communication in activation and nucleotide exchange. J Mol Biol. 2004; 338:469–481. [PubMed: 15081806]
29. Herrmann R, et al. Sequence of interactions in receptor-G protein coupling. J Biol Chem. 2004; 279:24283–24290. [PubMed: 15007073]
30. Herrmann R, et al. Rhodopsin-transducin coupling: role of the Galpha C-terminus in nucleotide exchange catalysis. Vision Res. 2006; 46:4582–4593. [PubMed: 17011013]
31. Oldham WM, Van Eps N, Preininger AM, Hubbell WL, Hamm HE. Mechanism of the receptor-catalyzed activation of heterotrimeric G proteins. Nat Struct Mol Biol. 2006; 13:772–777. [PubMed: 16892066]
32. Kapoor N, Menon ST, Chauhan R, Sachdev P, Sakmar TP. Structural evidence for a sequential release mechanism for activation of heterotrimeric G proteins. J Mol Biol. 2009; 393:882–897. [PubMed: 19703466]
33. Kaya AI, et al. A conserved phenylalanine as a relay between the alpha5 helix and the GDP binding region of heterotrimeric Gi protein alpha subunit. J Biol Chem. 2014; 289:24475–24487. [PubMed: 25037222]
34. Dror RO, et al. SIGNAL TRANSDUCTION. Structural basis for nucleotide exchange in heterotrimeric G proteins. Science. 2015; 348:1361–1365. [PubMed: 26089515]
35. Flock T, et al. Universal allosteric mechanism for Galpha activation by GPCRs. Nature. 2015; 524:173–179. [PubMed: 26147082]

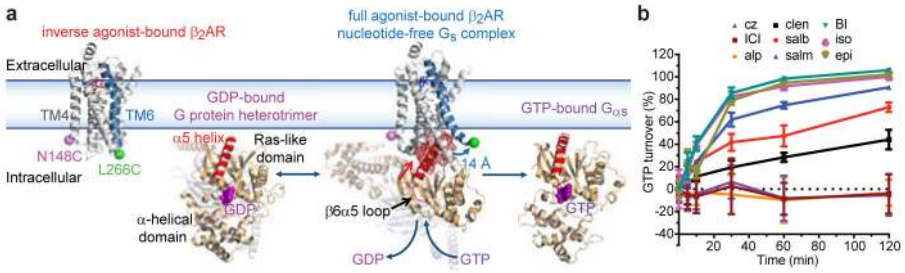

Figure 1.

High-resolution perspective of β_2AR-G_s activation. **a,** Labeling sites N148C (magenta) in TM4 and L266C (green) in TM6 (blue) are shown on the inactive β_2AR structure (PDB: 2RH1). Agonist activation leads to outward TM6 displacement (~14Å) and G_s coupling (shown GDP-bound G_i; PDB:1GP2). Within the GDP-free complex the α5 helix (red) of $G\alpha_s$ (wheat) engages the cytoplasmic face (red mesh) of β_2AR (PDB:3SN6). GTP binding causes $G\alpha_s$ (PDB:1AZT) and $G\beta\gamma$ subunit (not shown) to separate. **b,** Ligand efficacy profiles determined using a GTP turnover assay (**Methods**; error bars=s.e.m., 3 replicates).

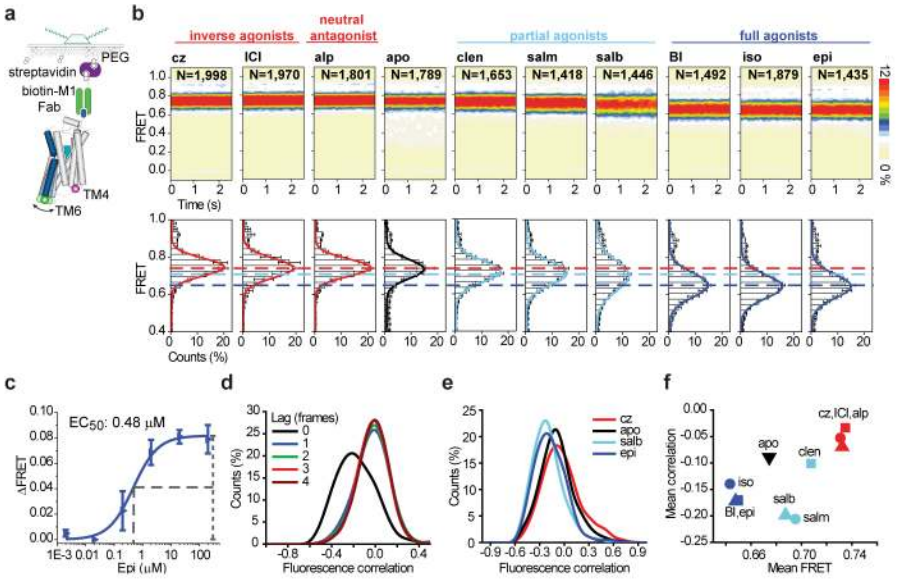

Figure 2.

The extent of TM6 motions correlate with efficacy. **a,** Schematic of ligand binding experiments (**Methods**). **b,** Population FRET contour plots (top; scale bar=relative population) and cumulative population histograms (bottom; error bars=s.d., 3 replicates with N total molecules). Dashed lines indicate the distinct mean FRET values observed. **c,** Apparent EC_{50} for epinephrine (**Methods**; error bars=s.d., 3 replicates). **d,** Pearson's correlation histograms (**Methods**) describing anticorrelated donor and acceptor fluorescence fluctuations in epinephrine with increasing donor lag time. **e,** Comparison of zero-lag Pearson's correlation histograms for representative ligands. **f,** Scatter plot of mean FRET efficiencies vs. mean correlation coefficients observed for each ligand.

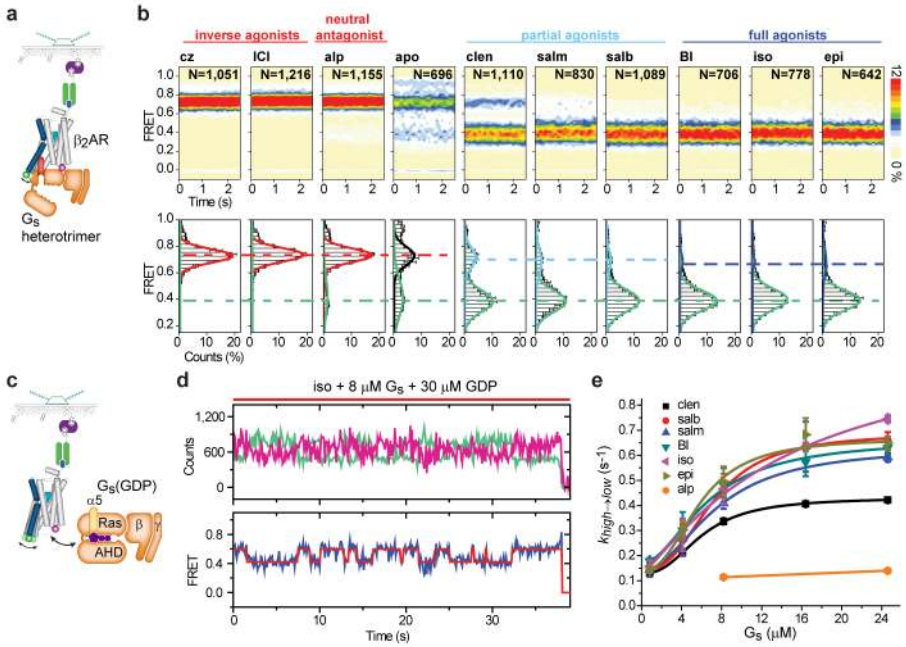

Figure 3.

Ligand efficacy affects β_2AR-G_s coupling efficiency. **a,** Schematic of G_s-coupling experiments (**Methods**). **b,** Population FRET contour plots (top; scale bar=relative population) and cumulative population histograms (bottom; error bars=s.d., 2 replicates with N total molecules) observed for apyrase-treated (nucleotide free) β_2AR-G_s complexes. Dashed lines show correspondence between high- and low-FRET values. **c,** Schematic of G_s titration experiments (**Methods**). **d,** Example fluorescence (donor [light green]; acceptor [magenta]), and FRET (blue) time traces overlaid with predicted state sequence (red) in the presence of iso, GDP and G_s. **e,** Transition rates from high- to low-FRET states ($k_{high \rightarrow low}$; error bars=s.d., 2 replicates) with increasing G_s(GDP) concentrations.

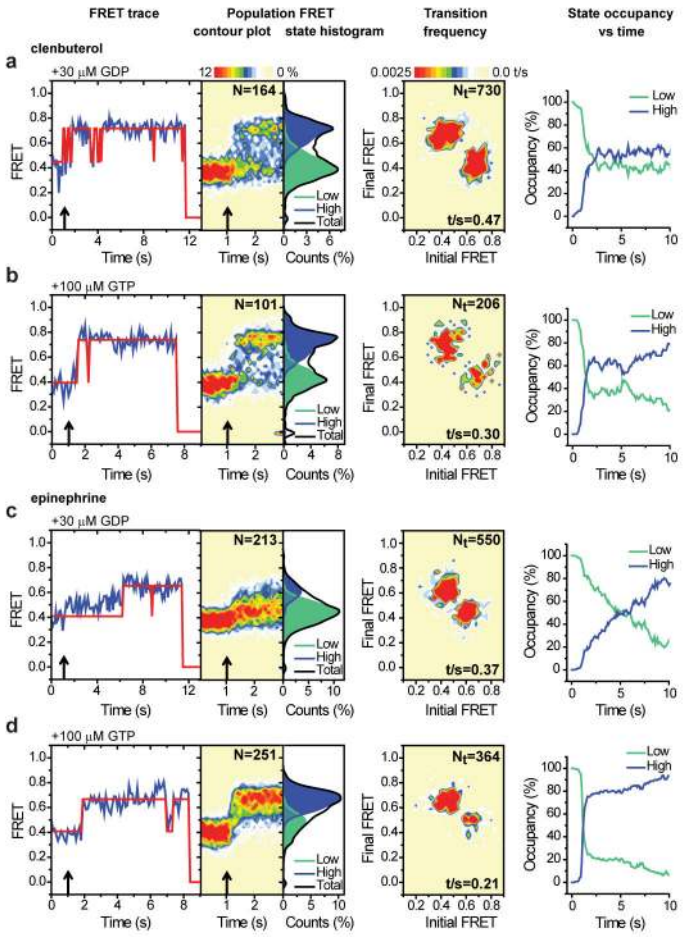

Figure 4.

Pre-steady state measurements of nucleotide binding to clen- and epi-bound β_2AR-G_s complexes. **a–d (panels from left to right),** Sample FRET traces (blue) with state idealizations (red line) following nucleotide addition (arrow). Population FRET contour plots (scale bar=relative population; N=total molecules) before and after nucleotide addition (arrow). Population histograms showing the relative occupancies of low- (green) and high- (blue) FRET states post-nucleotide addition. Transition density plots displaying the mean FRET values before (*x* axis) and after (*y* axis) each transition (scale bar=transitions per second t/s; N_t=total transitions). Time-dependent changes in the relative occupancies of low- (green) and high- (blue) FRET states.

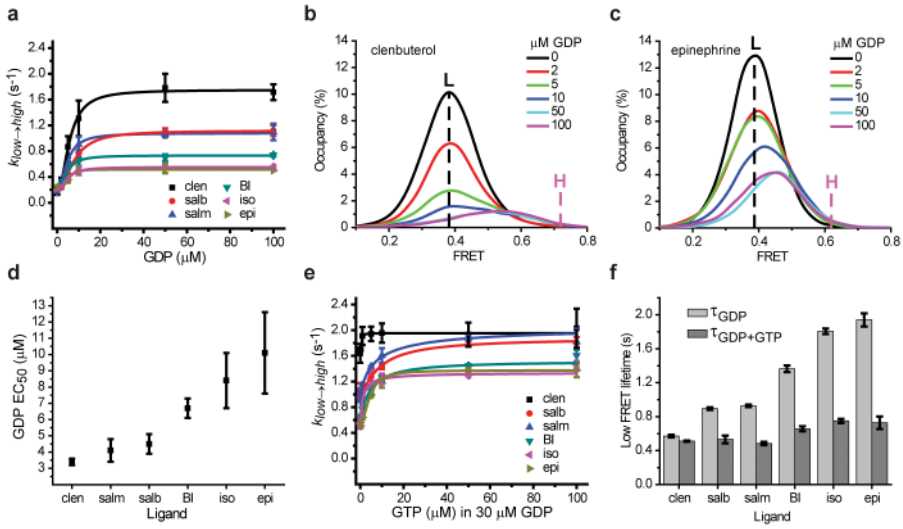

Figure 5.

Nucleotide exchange efficiency is ligand dependent. **a,** Transition rates from low- to high-FRET states ($k_{low \rightarrow high}$) with agonists, G_s and increasing GDP concentrations. **b–c,** Low-FRET state distributions with increasing GDP in G_s and clen (**b**) or epi (**c**). Vertical dashed lines indicate the mean low-FRET value observed without GDP (black; L) and the mean high-FRET value at 100 μM GDP (purple; H). **d**, Apparent EC_{50} for GDP binding to the β_2AR-G_s complex with different agonists. **e,** Transition rates from low- to high-FRET states ($k_{low \rightarrow high}$) with agonists, G_s, GDP, and increasing GTP concentrations. **f,** Histograms of low-FRET state lifetimes (τ) for each agonist with G_s and saturating GDP (light gray) or saturating GTP and GDP (dark gray). Error bars represents s.d. (two replicates) except (**d**), which represents s.e.m.

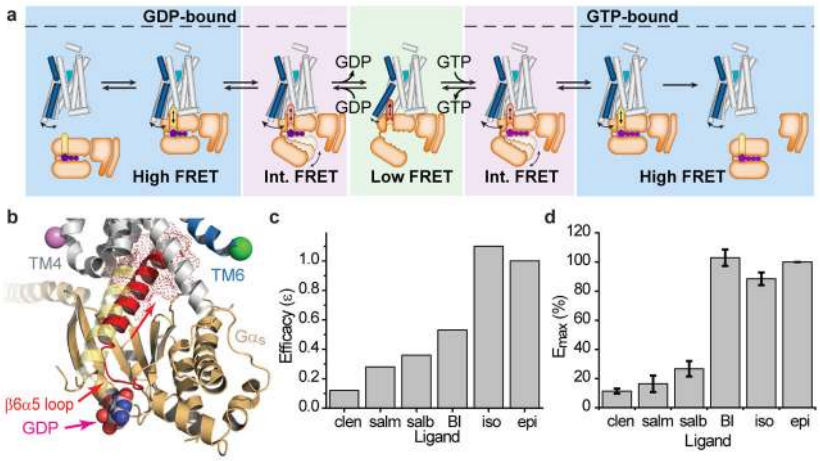

Figure 6.

Proposed kinetic framework underlying β_2AR-G_s coupling and nucleotide exchange. **a,** Schematic of β_2AR TM6 conformational states within the G protein activation cycle (Note: the low-FRET β_2AR-G_s(GTP) complex was not experimentally observed but is inferred). **b,** $G\alpha_s$ α5 helix engaging the intracellular face of β_2AR disrupts helix-proximal β6α5 loop interactions with GDP. **c,** Ranking of agonist molecular efficacies (ε) relative to epi in terms of the effective rate of generating G_s(GTP) from G_s(GDP) (**Methods**). **d,** Ligand efficacy-based cAMP measurements in living cells (**Methods**; error bars=s.e.m, 3 replicates).